



# Formation of a single drop of molten steel following bursting of liquid film in a vertical steel plate illuminated by a high energy laser

M. Y. Lanzerotti<sup>1</sup> · K. Brakke<sup>2</sup> · K. Allen<sup>3</sup> · W. Blackmon<sup>4</sup> · J. Hartke<sup>3</sup> · Amir H. Hirs<sup>5</sup>

Received: 19 March 2021 / Accepted: 8 June 2021 / Published online: 30 July 2021  
© The Author(s), under exclusive licence to Springer-Verlag GmbH, DE part of Springer Nature 2021

## Abstract

The formation and dynamics of a single drop of liquid under the influence of gravity can be experienced as everyday phenomena, and have been the subject of scientific investigations since at least the work of Leonardo da Vinci in the early 1500s and Mariotte in the 1680s. Experiences with liquid drops in everyday life are captured by poets and artists as well as scientists, whose theoretical and experimental investigations develop fundamental understanding of drops with size  $< 1$  mm to  $> 10^7$  m. This paper presents observations of the formation of a single liquid drop of molten steel following bursting of a liquid film formed by illuminating a steel plate by a high energy laser. The hole morphology is analyzed with a proposed kinematic model of hole expansion for the very early stages in the bursting of the hole. Estimates of the hole eccentricity, area, perimeter, and circularity obtained from the model are presented and discussed. Experimental measurements show that a single drop of liquid steel detaches from the end of a neck that then cools to room temperature. Measurements also show that the liquid drop oscillates while falling under gravity. No satellite drops are observed.

**Keywords** Laser drop formation · Thick liquid film · Hole formation

## 1 Introduction

This work generates a liquid drop with the use of a vertical metal sheet. The question of the creation and dynamics of a single drop of liquid under the influence of gravity has focused primarily on the formation at room temperature conditions and can be experienced in typical activities of daily life. A “drop of water” [1, 2] can be observed, for example, by opening and closing a faucet. Inspiration in nature

is found in raindrops ( $\sim 1$  mm) [3], in limestone stalactites growing from a single “mineral-laden drop of water” [4], and in Lord Kelvin’s 1862 estimate [5]–[9] of the age of Earth ( $> 10^7$  m). Knowledge gained is applied to developing inkjet printing technologies reviewed by Cummins and Desmulliez [10], measuring liquid properties such as surface tension [11]–[18], and dating the 500,000-year history of the Siberian permafrost [19].

Da Silva *et al.* have investigated the acceleration of metal drops in a laser beam [20], and Bowering *et al.* have studied the behavior of metal drops on silicon wafers [21]. Applications for the research are in a wide range of areas including applying laser drop generation currently used to produce liquid drops from metal wires and rods [20–26]. Additional applications are in laser welding [27], laser welding in the automotive industry [28], consumer goods such as refrigerators [29] and washing machine baskets [30], and defense applications [31–35].

More recent printing methods in additive manufacturing for metal droplet 3D printing have been developed by He *et al.* [36], Deng *et al.* [37], and Hou *et al.* [38]. He *et al.* [36] demonstrated droplet-based 3D printing with aluminum droplets. He *et al.* “establishes a specific droplet scanning strategy” [36] and directly fabricated aluminum

✉ M. Y. Lanzerotti  
marylanzerotti@vt.edu

<sup>1</sup> Department of Electrical and Computer Engineering, Virginia Polytechnic Institute & State University, Arlington, VA, U.S.A.

<sup>2</sup> Department of Mathematics and Computer Science, Susquehanna University, Selinsgrove, PA, U.S.A.

<sup>3</sup> Department of Physics and Nuclear Engineering, United States Military Academy, West Point, NY, U.S.A.

<sup>4</sup> Department of Civil and Mechanical Engineering, United States Military Academy, West Point, NY, U.S.A.

<sup>5</sup> Department of Mechanical, Aerospace, and Nuclear Engineering, Rensselaer Polytechnic Institute, Troy, NY, U.S.A.

tube structures with variable cross sections and with the use of dissolvable supports. Deng *et al.* [37] first quantified the size and toroid shape of gas pinholes formed following the impact of molten droplets of an aluminum alloy on solid brass substrates. Using the fundamental studies of Deng *et al.* [37], researchers in additive manufacturing may be better able to predict defects arising from gas pinholes. Hou *et al.* [38] took into account for the first time the presence of solidified aluminum droplets in investigations of neighboring aluminum droplets during remelting and horizontal droplet deposition. Hou *et al.* [38] focused specifically on obstructions caused by ripples and solidification angles of the solidified aluminum droplets on remelting of molten droplets. Further, Hou *et al.* demonstrated that simulations of this process show good agreement with experiments [38].

The behavior of a water drop has been studied at least since 1508 beginning with the work of Leonardo da Vinci (“goccia d’acqua”), who mentioned the neck returning upwards after a water drop detached [39]–[42] Edmé Mariotte (“goutte d’eau”) in 1686 [43], Johann Segner in 1751 [44], Pierre-Simon Laplace and Thomas Young in 1805 [45, 46], Félix Savart in 1833 [47, 48], and T. Tate (“drop of Water”) in 1864 [49]. The formation of a liquid drop under the influence of gravity has been studied theoretically [52, 54, 56–61] and experimentally [50]–[55, 59, 61–66] as, for example, in pendant drops [67] jets [68–73], and dripping faucets [74–78].

The oscillation of a drop of liquid [79]–[90] has been studied since the 1880s by Horace Lamb [79], Lord Kelvin [80], and Lord Rayleigh [81, 82], who obtained an expression for the fundamental oscillation mode (Rayleigh frequency) of a spherical liquid drop given by [90]  $\omega_R = \sqrt{\frac{8\sigma}{\rho R^3}}$ , where  $\sigma$ ,  $\rho$  and  $R$  represent the surface tension, density, and mean radius of the drop, respectively [90]. Oscillations have also been studied in double droplet systems [91]–[93].

This work presents experimental observations of formation by laser heating of a single liquid drop, with no satellite drops, following the bursting of a thick vertical liquid film of molten steel in a vertical steel plate (in which the molten region was formed). “Between melting and freezing” [94] of the steel, the molten steel descends from a vertical liquid film, forming a liquid drop that is not in thermal equilibrium with ambient room temperature conditions. The flow of the liquid from the hole rim (referred to as the hoop herein) is more similar to the flow of liquid from one end of a horizontal pipe; the molten steel flows out the hoop toward the front of the steel plate (facing the high energy laser). Bursting occurs in the upper portion of the film, not in the center, as a dimple thins to zero thickness due to draining of fluid. The neck that produces the drop solidifies rapidly as it cools to room temperature. Specific application scenarios for this work are in the development of models to describe

the interactions of high energy lasers with metal targets such as mortar rounds and UAVs [31–35].

The contributions of this paper are a description of the neck and drop formation process, tracking data of the neck and drop formation process as well as the falling drop, a rough estimate of the surface tension of molten steel from a falling oscillating drop, a proposed kinematic model of hole formation, and a discussion of the hole morphology including physical characteristics such as hole perimeter, hole area, hole circularity, and hole eccentricity.

## 2 Experimental

### 2.1 Materials and setup

The experiments are conducted with 1.5-mm-thick vertical cold rolled ASTM A1008 (6sh16) steel sheets. The steel sheets are imaged by an IDT Os7 high-speed camera operating at 3000 fps at room temperature (Fig. 1). Figure 2 shows the target geometry for a vertical target with thickness  $d$  and target at zero incidence angle. Figure 2a and b shows the target. The unit vectors are  $(\hat{x}, \hat{y}, \hat{z})$ , and the three-dimensional coordinate system  $\{x, y, z\}$  is also shown. The angle  $\theta$  is taken within the plane of the plate to take on positive values in the counterclockwise direction (Fig. 2).

### 2.2 Heating

The vertical film of molten steel is created by illuminating a 1.5-mm-thick vertical cold rolled ASTM A1008 (6sh16) steel sheet with a 1-kW, 1075-nm YLR-1000 infrared laser.

### 2.3 Samples

The steel sheet is cut in the machine shop with a size of approximately 6 inches x 3 inches to fit in the holder placed in front of the laser beam.

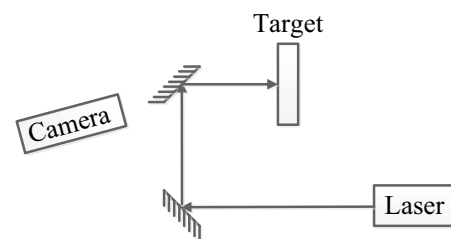
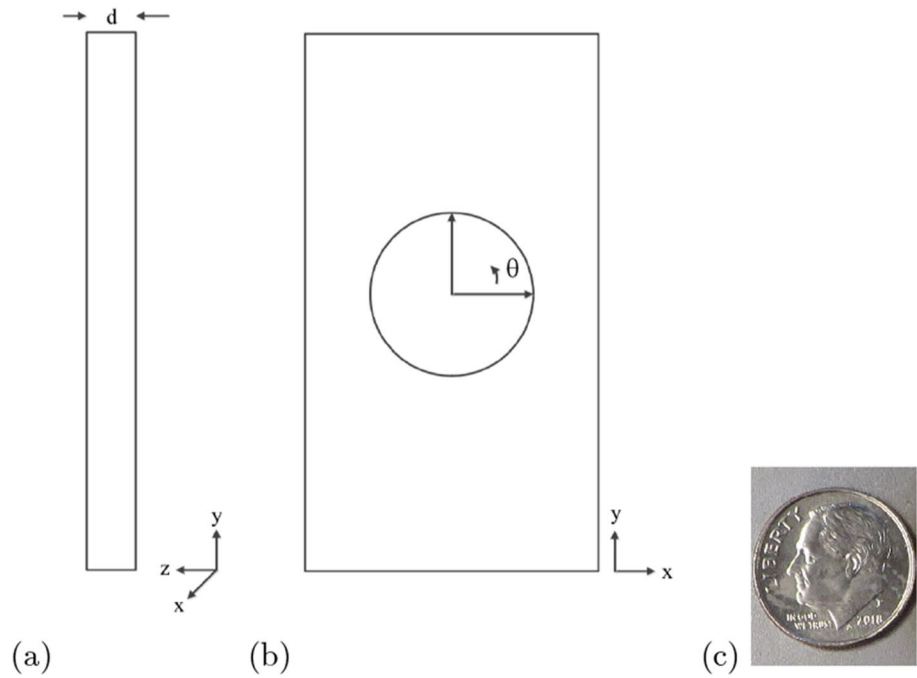


Fig. 1 Experimental setup [95] “Reproduced from Lanzerotti *et al.*, *Appl. Phys. Lett.* vol. 115, (2019), with the permission of AIP Publishing.”

**Fig. 2** Target geometry. Side view **a** and front view **b** of vertical target with **c** a US dime for size comparison. The laser propagates in the negative  $\hat{z}$  direction



### 3 Results

#### 3.1 Hole formation

Table 1 and Fig. 3 present observations and photographs, respectively, of the hole, neck, and drop formation process. The laser was turned off at the right moment before the film burst so the film could be photographed. The photographs show that the film persists as a molten disk (Table 1, Step 1) after the laser is turned off (Table 1, Step 0) before the

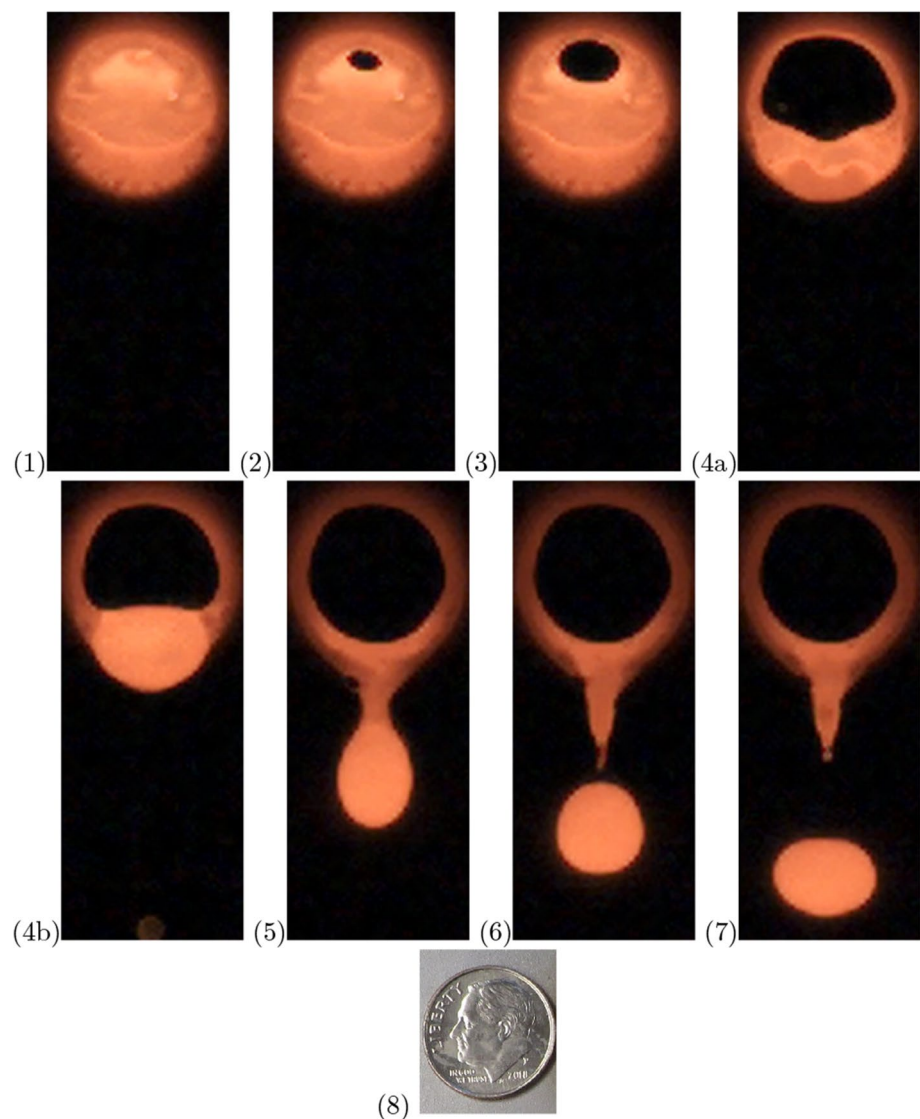
film ruptures (Table 1, Step 2). Gravity is responsible for the formation of a dimple and bulge in the liquid; there is an equilibrium between gravity and surface tension (Table 1, Step 1). If the front and back dimples become deep enough to meet, then a hole forms and rapidly expands (Table 1, Step 2). Fig. 3-1 shows a photograph of the frame just prior to ( $\frac{1}{3}$  ms) the first appearance of the hole in Fig. 3-2. Surface tension rapidly expands the hole (Table 1, Step 3).

Figure 3 shows a comparison of the initial position of the hole in Fig. 3-(2) with the final hole in Fig. 3-(7). The initial hole is located approximately 27 pixels ( $\approx 3.3$  mm)

**Table 1** Formation of liquid drop

Step	Observation	Time (s)	Interpretation
0	Laser off	–	–
1	Dimple and bulge persist as a molten disk within hoop (Fig. 3-1)	–	Near equilibrium between gravity and surface tension as fluid drains
2	Liquid film ruptures (Fig. 3-2)	0	Dimple thins to zero thickness due to draining of fluid
3	Hole expands (Fig. 3-3)		Surface tension rapidly expands hole
4a	Liquid flows into spherical lump at lower part of hole (Fig. 3-4a)	0-0.1040	–
4b	Liquid vibrates twice at lower part of hole (Fig. 3-4b)	0-0.1040	–
5	Liquid drop forms below hoop rim; liquid neck forms below hoop lower rim (Fig. 3-5)	0.1040 to 0.1700	Gravity finally has the time to pull the liquid down
6	Drop detaches (Fig. 3-6)	0.1700	The neck pinches off
	Neck rear retracts	0.1700-0.1703	Tiny retraction of neck before it freezes
	Neck front retracts	0.1700-0.1710	
	Tiny droplet appears to form at bottom of neck	0.1700-0.1727	Tiny droplet solidifies without detaching
7	Drop falls under gravity (Fig. 3-7)	0.1727-0.2263	Falling drop oscillates
8	Drop stops falling	0.2263	Drop hits mount surrounding steel plate

**Fig. 3** Photographs of formation of a liquid drop taken by a high-speed digital camera of the visible light emitted by the hot molten steel. Photographs 1-7 correspond to Steps 1-7 (Table 1), respectively, with (8) a US dime for size comparison. Photographs 1, 2, 3, 6 are “Reproduced from Lanzerotti *et al.*, *Appl. Phys. Lett.* vol. 115, (2019), with the permission of AIP Publishing.” A comparison of the initial position of the hole in (2) with the final hole in (7) shows that the initial hole is off-center compared with the final hole. The off-center position of the initial hole is also shown in the tracking data at location (0,0), which is located approximately 27 pixels above the hole center, in Fig. 4



above the final hole center, as can be seen in the tracking data in Fig. 4a.

Figure 4 shows the tracking positions of hole, neck, and falling drop, showing the position that the hole bursts in the thick molten film (Fig. 3-(2)) located at (0, 0) pixels (75 pixels per 9.53 mm). The off-center position of the initial hole is shown in the tracking data in position (0,0) that is approximately 27 pixels above the center of the final hole (Fig. 4a). These photographs show that the initial bursting location is off-center with respect to the final hole formed by the laser beam.

### 3.2 Neck and drop formation

The molten liquid gathers into a spherical lump at the lower part of the hole (Table 1, Step 4a). Surface tension tends to make the liquid form into spheres; the lump is at the lower part of the hoop rim, since that is where the bulge was with

the bulk of the liquid (Table 1, Step 4a). The liquid lump vibrates twice at the lower part of the hole (Table 1, Step 4b), as it settles into a sphere, before descending further as gravity has time to pull the liquid down to form a neck of molten steel between the hoop rim and the drop (Table 1, Step 5). The molten liquid drains preferentially at the front of the sheet (Figs. 6, 7a).

Tracking data obtained from photographs (Fig. 8) show that the neck width decreases (Fig. 5) and takes on its smallest value just prior to drop detachment. Photographs (Figs. 6, 7, 8) also show asymmetry in the neck in the front of the 9.88-mm-diameter hole (Fig. 7a) and hole rear (Fig. 7b) in the 1.5-mm-thick steel plate. A front view of the neck (at the front of the steel plate illuminated by the laser) is shown in Fig. 7a, and a rear view of the hole (the back of the steel plate) is shown in Fig. 7b. A comparison of Fig. 7a and b shows that the molten liquid drained preferentially at the front of the sheet.

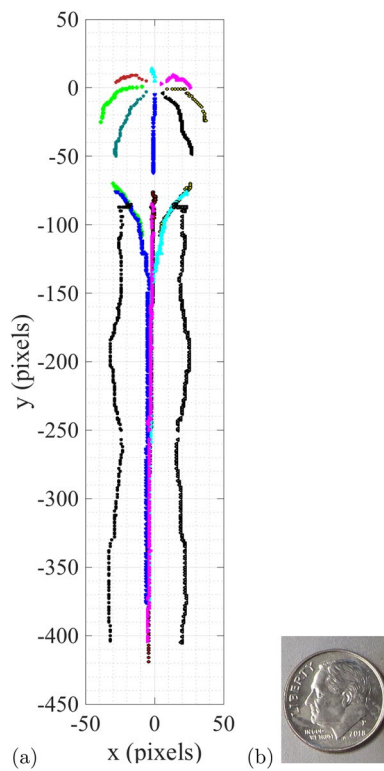


**Fig. 4** **a** Tracking positions of hole, neck, and falling drop, showing the position that the hole bursts in the thick molten film (Fig. 3-2) located at (0,0) pixels (75 pixels per 9.53 mm). This position is off center relative to the center of the hole, which is located approximately 27 pixels lower. **b** shows a US dime for size comparison

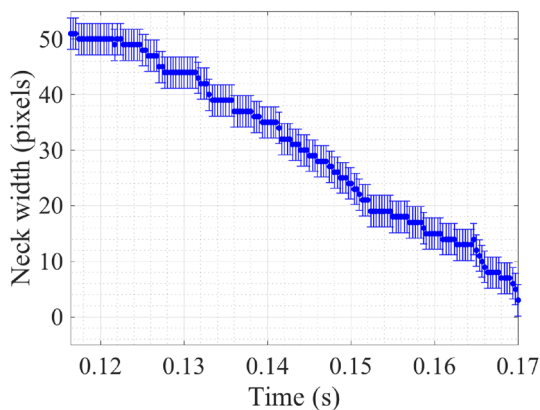


**Fig. 5** Neck width as a function of time after hole rupture (Table 1, Step 2). Drop detaches from neck at time  $t = 0.1700$  s (Table 1, Step 6)

The first appearance of the detached drop is shown in Fig. 3-(6) (Table 1, Step 6). The neck retracts upward slightly before freezing, with a small droplet that appears to form at the bottom of the neck (before the neck freezes) but does not detach (Table 1, Step 6; Fig. 3-(7)).



**Fig. 6** A photograph taken with a Canon PowerShot digital camera shows a front view of the neck below the rim of a 9.88-mm-diameter hole in a 1.5-mm-thick steel plate, showing molten liquid draining preferentially at the front face of the sheet. A US dime (10-cent coin) is included for size comparison

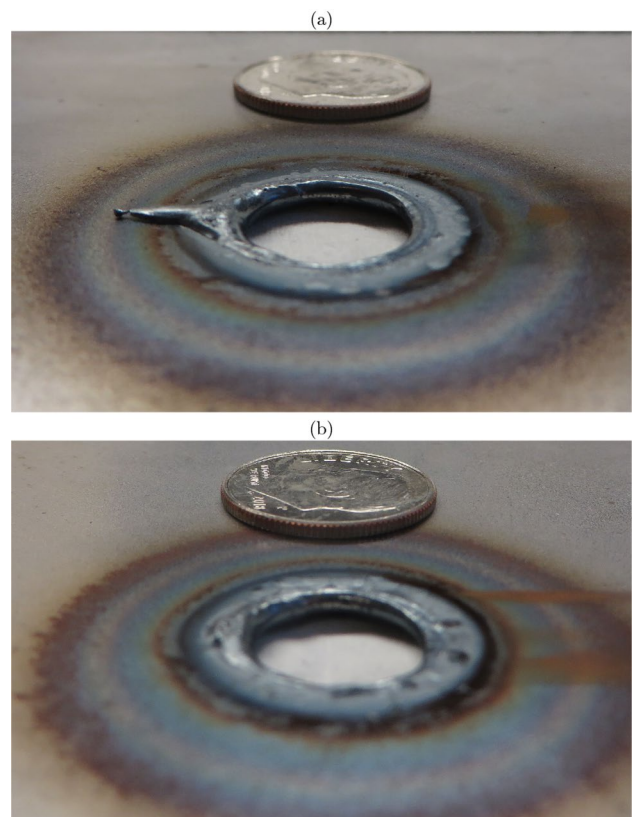


**Fig. 7** Photographs taken with a Canon PowerShot digital camera show oblique views of **a** the front face of the sheet with the neck formed after molten liquid drained preferentially at the front of the sheet, and **b** the back face. A US dime (10-cent coin) is included for size comparison

**Fig. 8** Photographs taken at 3000 fps by a high-speed camera of the visible light emitted by the hot molten steel showing a falling drop, with tracking using MotionStudio software. Time intervals between photographs are  $\Delta t_{ab} = t_a - t_b \approx 5.33$  ms;  $\Delta t_{bc} = t_b - t_c \approx 5.67$  ms;  $\Delta t_{cd} = t_c - t_d \approx 6.33$  ms;  $\Delta t_{de} = t_d - t_e \approx 7.67$  ms;  $\Delta t_{ef} = t_e - t_f \approx 7.67$  ms;  $\Delta t_{fg} = t_f - t_g \approx 3.67$  ms;  $\Delta t_{gh} = t_g - t_h \approx 2.67$  ms. (i) shows a US dime for size comparison

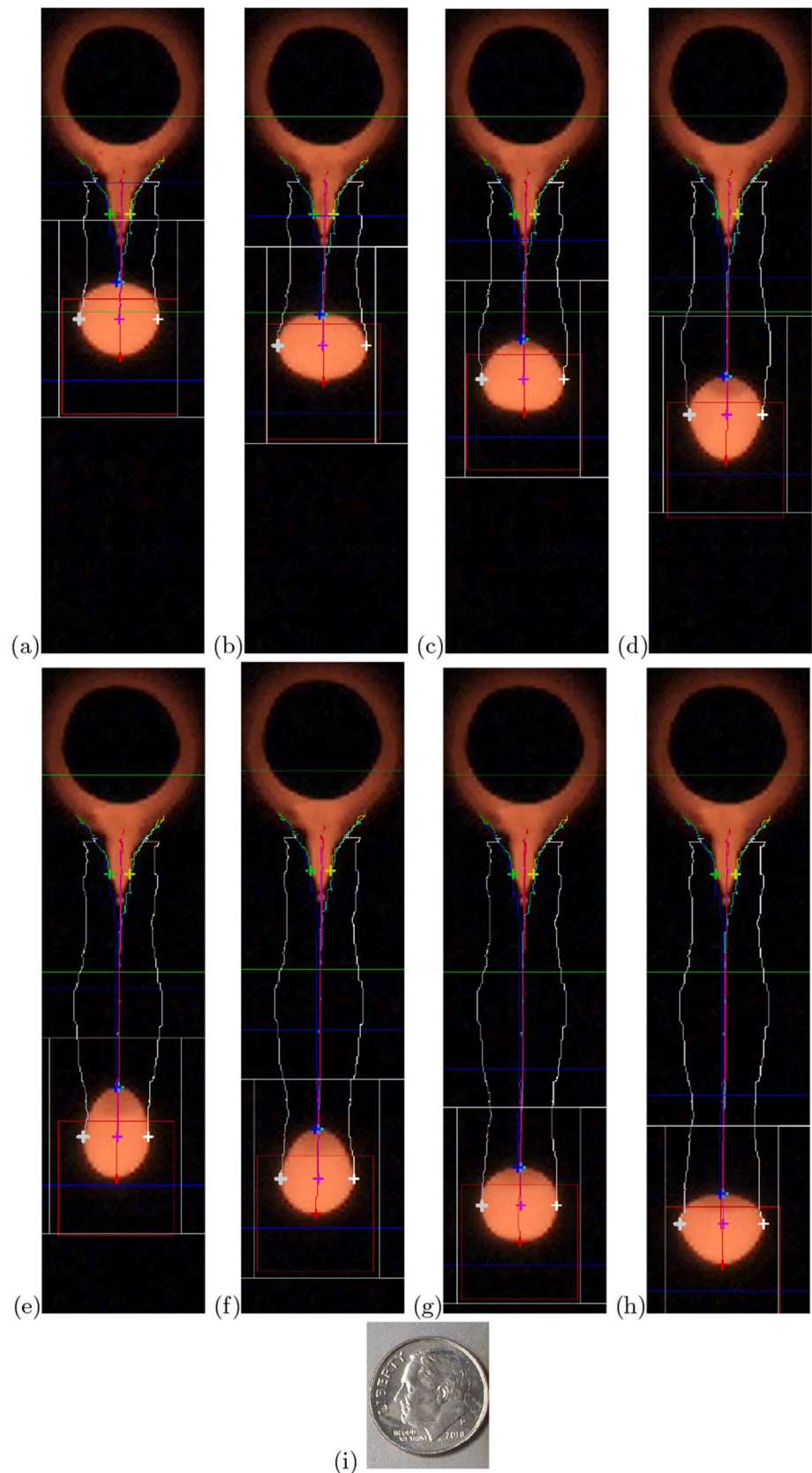


**Fig. 9** **a** Center, **b** width, **c** height, **d** aspect ratio of falling drop ▶ (Table 1, Step 7)

### 3.3 Falling drop

Photographs (Fig. 8) show that the drop then falls under gravity, and tracking data (Fig. 4) obtained from the photographs show that the drop shape oscillates (Figs. 8, 9) as the drop falls under gravity (Table 1, Step 7), with aspect ratio as high as ~ 1.5 during the fall (Fig. 9d). The drop oscillates without appearing to hit the vertical steel plate. Images of the falling drop captured by the high-speed camera and tracking data from the trajectory of the center of the drop show that the position of the drop (Figs. 8, 9) is farther from the hole as time increases, as expected in gravity. The drop stops falling when it hits the mount surrounding the steel plate (Table 1, Step 8), after Fig. 8h, approximately one oscillation of the drop.

A rough estimate of the surface tension  $\sigma \sim (150 \pm 20) \frac{mN}{m}$  is obtained (Table 2) from measurements of the mean radius  $R$  of the oscillating molten steel drop (Fig. 9), period  $T$  of drop oscillation (Fig. 9), with  $\sigma = \frac{\omega^2 \rho_L R^3}{8}$  (Eqn. 1.1, Rayleigh frequency [90]). The density of liquid iron is estimated [96, 97] as  $\rho_L = 5810 \frac{kg}{m^3}$  by evaluating Nishizuka’s [96] expression cited by Morohoshi (Eq. 10 in [97]) at 3134 K.

Scans of the deflection of the steel plate are acquired with a Chicago dial mechanical indicator CD1 with the steel plate mounted horizontally in a Haas TM-1 vertical milling machine. The data from the scans show minimal deflection after the plate cools to room temperature (Fig. 10).

## 4 Hole morphology

### 4.1 Kinematic model of hole formation

When the hole bursts at time  $t = t_h$ , the initial speed  $v_{h, \text{ellipse}}(\theta)$  of the hole perimeter is a function of the angle  $\theta$  relative to the horizontal (Fig. 2). In this situation, the angular dependence of the initial speed of the expanding hole may be written as,

$$v_{t_h, \text{ellipse}}(\theta) = \frac{v_{a, \text{ellipse}} v_{b, \text{ellipse}}}{\sqrt{v_{a, \text{ellipse}}^2 (\sin \theta)^2 + v_{b, \text{ellipse}}^2 (\cos \theta)^2}} \quad (1)$$

where the terms  $v_{a, \text{ellipse}}$  and  $v_{b, \text{ellipse}}$  represent the initial speeds along the horizontal semi-major axis and vertical semi-minor axis, respectively.

The velocity vectors  $\mathbf{v}_{\text{ellipse}}(\theta, t)$  and position vectors  $\mathbf{r}_{\text{ellipse}}(\theta, t)$  for a proposed ellipse model of hole expansion as functions of time  $t \geq t_h$  can be written as,

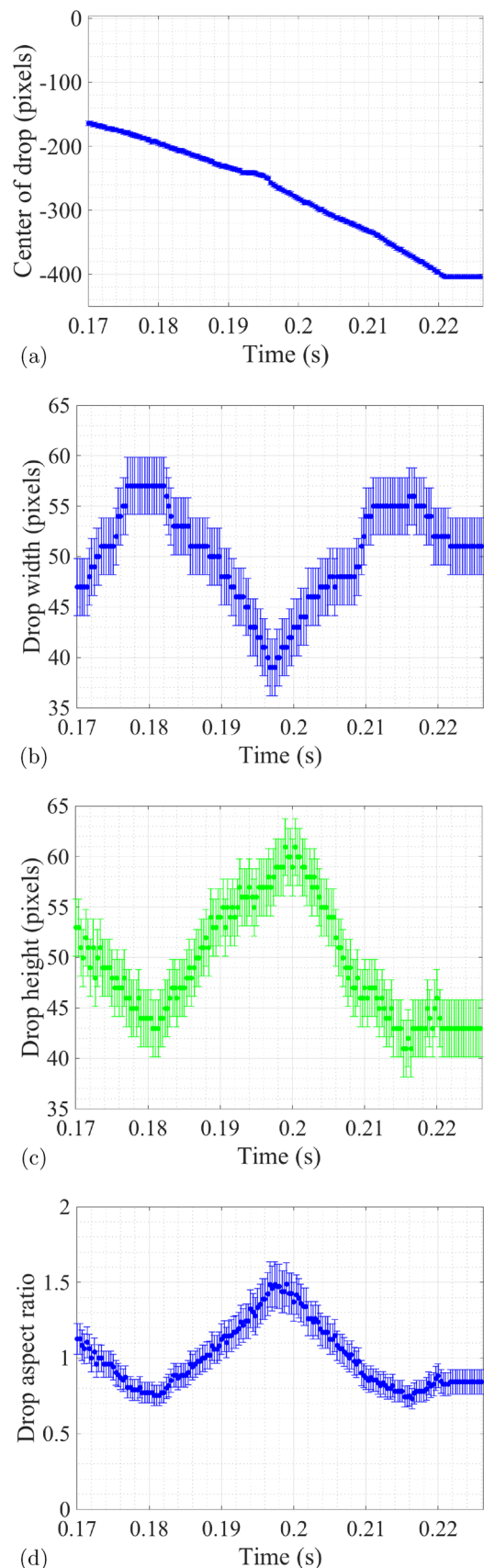


**Table 2** Estimate of surface tension of molten steel obtained from measurements of oscillation frequency of falling drop (Table 1, Step 7) and mean radius of spherical drop (Table 1, Step 7)

Parameter	Estimate
Period of oscillation, $T$ (Figs. 8, 9)	$T \sim (0.035 \pm 0.001) \text{ s}$
Frequency of oscillation, $\omega_R$	$\omega_R \sim \frac{1}{2\pi} (180 \pm 5) \frac{1}{\text{s}}$
Mean radius of spherical drop, $R$ (Fig. 9)	$R \sim (50 \pm 3) \text{ pixels}$
Surface tension of drop, $\sigma$	$\sigma \sim (150 \pm 20) \frac{\text{mN}}{\text{m}}$

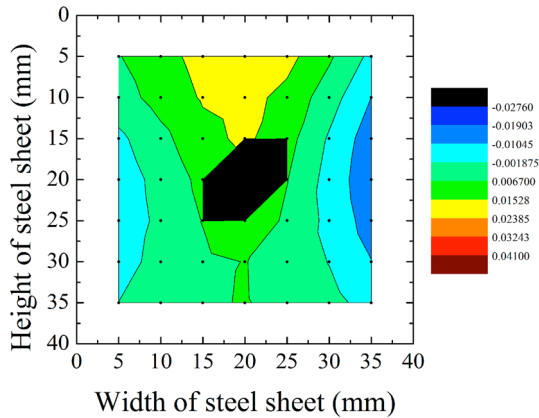


**Fig. 10** Deflection out of the plane of the steel sheet with hole (Fig. 1b) measured by tracing a Chicago dial mechanical indicator CD1 (microns) across the surface of the steel plate. The steel plate is mounted horizontally in a Haas TM-1 milling machine. The black region shows where measurements were not taken (in the hole)

$$\begin{aligned}
 \mathbf{v}_{\text{ellipse}}(\theta, t) &= v_{t_h, \text{ellipse}}(\theta)(\cos \theta)\hat{x} \\
 &+ \left( v_{t_h, \text{ellipse}}(\theta)(\sin \theta) + a_{y, \text{ellipse}}t \right)\hat{y}, \\
 \mathbf{r}_{\text{ellipse}}(\theta, t) &= \left\{ x_{t_h}(\theta) + v_{t_h, \text{ellipse}}(\theta)(\cos \theta)t \right\}\hat{x} \\
 &+ \left\{ y_{t_h}(\theta) + v_{t_h, \text{ellipse}}(\theta)(\sin \theta)t + \frac{1}{2}a_{y, \text{ellipse}}t^2 \right\}\hat{y}.
 \end{aligned} \tag{2}$$

**Table 3** Table of parameters for ellipse model of hole formation

Parameter	Parameter values $\left( \frac{\text{pixels}}{\text{s}}, \frac{\text{pixels}}{\text{s}^2} \right)$	Parameter values $\left( \frac{\text{m}}{\text{s}}, \frac{\text{m}}{\text{s}^2} \right)$
$\tilde{v}_{t_h, x, 0^\circ}$	$(5, 300 \pm 360) \frac{\text{pixels}}{\text{s}}$	$(0.650 \pm 0.044) \frac{\text{m}}{\text{s}}$
$\tilde{v}_{t_h, x, 180^\circ}$	$-(3, 500 \pm 340) \frac{\text{pixels}}{\text{s}}$	$-(0.430 \pm 0.040) \frac{\text{m}}{\text{s}}$
$\tilde{v}_{t_h, y, 90^\circ}$	$(1, 900 \pm 300) \frac{\text{pixels}}{\text{s}}$	$(0.230 \pm 0.037) \frac{\text{m}}{\text{s}}$
$\tilde{v}_{t_h, y, 270^\circ}$	$-(5, 100 \pm 290) \frac{\text{pixels}}{\text{s}}$	$-(0.630 \pm 0.036) \frac{\text{m}}{\text{s}}$
$\tilde{a}_{t_h, y, 90^\circ}$	$-(240, 000 \pm 89, 000) \frac{\text{pixels}}{\text{s}^2}$	$-(29 \pm 11) \frac{\text{m}}{\text{s}^2}$
$\tilde{a}_{t_h, y, 270^\circ}$	$-(530, 000 \pm 85, 000) \frac{\text{pixels}}{\text{s}^2}$	$-(65 \pm 10) \frac{\text{m}}{\text{s}^2}$
Parameter	Ellipse model $\left( \frac{\text{pixels}}{\text{s}}, \frac{\text{pixels}}{\text{s}^2} \right)$	Ellipse model $\left( \frac{\text{m}}{\text{s}}, \frac{\text{m}}{\text{s}^2} \right)$
$\tilde{v}_{a, \text{ellipse}}$	$(4, 400 \pm 1, 300) \frac{\text{pixels}}{\text{s}}$	$(0.54 \pm 0.16) \frac{\text{m}}{\text{s}}$
$\tilde{v}_{b, \text{ellipse}}$	$(2, 600 \pm 990) \frac{\text{pixels}}{\text{s}}$	$(0.32 \pm 0.12) \frac{\text{m}}{\text{s}}$
$\tilde{a}_{y, \text{ellipse}}$	$-(390, 000 \pm 200, 000) \frac{\text{pixels}}{\text{s}^2}$	$-(47 \pm 25) \frac{\text{m}}{\text{s}^2}$

Least-squares linear fits to the measurement tracking data for the  $x$ -components of the position vector,  $\mathbf{r}_{\text{hole}}(\theta = 0^\circ, t)$  and  $\mathbf{r}_{\text{hole}}(\theta = 180^\circ, t)$ , and least-squares quadratic fits to the tracking data for the  $y$ -component of the position vector,  $\mathbf{r}_{\text{hole}}(\theta = 90^\circ, t)$  and  $\mathbf{r}_{\text{hole}}(\theta = 270^\circ, t)$ , for  $t_h \leq t \leq (t_h + 4) \text{ ms}$  can be written with fit parameter estimates  $\{ \tilde{v}_{t_h, x, 0^\circ}, \tilde{v}_{t_h, x, 180^\circ}, \tilde{v}_{t_h, y, 90^\circ}, \tilde{a}_{t_h, y, 90^\circ}, \tilde{v}_{t_h, y, 270^\circ}, \tilde{a}_{t_h, y, 270^\circ} \}$  (Table 3), as

$$\begin{aligned}
 x_{\text{hole}}(\theta = 0^\circ, t) &= \left\{ (5, 300 \pm 360) \frac{\text{pixels}}{\text{s}} \right\} t, \\
 &= \tilde{v}_{t_h, x, 0^\circ} t,
 \end{aligned} \tag{3}$$

$$\begin{aligned}
 x_{\text{hole}}(\theta = 180^\circ, t) &= \left\{ -(3, 500 \pm 340) \frac{\text{pixels}}{\text{s}} \right\} t, \\
 &= \tilde{v}_{t_h, x, 180^\circ} t,
 \end{aligned} \tag{4}$$

$$\begin{aligned}
 y_{\text{hole}}(\theta = 90^\circ, t) &= \left\{ (1, 900 \pm 300) \frac{\text{pixels}}{\text{s}} \right\} t \\
 &+ \left\{ -(240, 000 \pm 89, 000) \frac{\text{pixels}}{\text{s}^2} \right\} t^2, \\
 &= \tilde{v}_{t_h, y, 90^\circ} t + \tilde{a}_{t_h, y, 90^\circ} t^2,
 \end{aligned} \tag{5}$$

$$\begin{aligned}
 y_{\text{hole}}(\theta = 270^\circ, t) &= \left\{ -(5, 100 \pm 290) \frac{\text{pixels}}{\text{s}} \right\} t \\
 &+ \left\{ -(530, 000 \pm 85, 000) \frac{\text{pixels}}{\text{s}^2} \right\} t^2, \\
 &= \tilde{v}_{t_h, y, 270^\circ} t + \tilde{a}_{t_h, y, 270^\circ} t^2.
 \end{aligned} \tag{6}$$

We assume constant initial speed of hole expansion along the semi-major axis and constant initial speed along the semi-minor axis (the two initial speeds may take on different values). We then calculate the average of the fit parameters obtained from least squares linear fits to the first five data points of the  $x$ -component of the tracking data with  $\theta = \{0^\circ, 180^\circ\}$  to obtain an estimate of the initial speed



$\tilde{v}_{a,ellipse}$  along the semi-major axis. Next, we calculate the average of the fit parameters of the linear term obtained from least squares quadratic fits to the first five data points of the  $y$ -component of the tracking data with  $\theta = \{90^\circ, 270^\circ\}$  to obtain an estimate of the initial speed  $\tilde{v}_{b,ellipse}$  along the semi-minor axis. These can be expressed as,

$$\begin{aligned} \tilde{v}_{a,ellipse} &= \frac{1}{2}(|\tilde{v}_{t_h,x,0^\circ}| + |\tilde{v}_{t_h,x,180^\circ}|), \\ \tilde{v}_{b,ellipse} &= \frac{1}{2}(|\tilde{v}_{t_h,y,90^\circ}| + |\tilde{v}_{t_h,y,270^\circ}|), \end{aligned} \tag{7}$$

respectively.

We obtain an estimate of the acceleration in the  $y$ -direction  $\tilde{a}_{t_h,y,ellipse}$  by taking the average of the acceleration obtained from the fit to the position data vertically above the hole and below the hole, such that,

$$\tilde{a}_{y,ellipse} = \frac{1}{2}(\tilde{a}_{t_h,y,90^\circ} + \tilde{a}_{t_h,y,270^\circ}), \tag{8}$$

where we assume that the vertical acceleration is constant at the points in time at the earliest stage of hole expansion. Substituting values for the fit parameters in Table 3 into Eqns. 7 and 8, we obtain values for estimates  $\tilde{v}_{a,ellipse}$ ,  $\tilde{v}_{b,ellipse}$ , and  $\tilde{a}_{y,ellipse}$ , as

$$\tilde{v}_{a,ellipse} = (4,400 \pm 1,300) \frac{\text{pixels}}{\text{s}}, \tag{9}$$

$$\tilde{v}_{b,ellipse} = (2,600 \pm 990) \frac{\text{pixels}}{\text{s}}, \tilde{a}_{y,ellipse} = -(390,000 \pm 200,000) \frac{\text{pixels}}{\text{s}^2}. \tag{10}$$

These estimates can be used to obtain an estimate of the initial speed of the hole perimeter  $\tilde{v}_{t_h,ellipse}(\theta)$  according to

$$\tilde{v}_{t_h,ellipse}(\theta) = \frac{\tilde{v}_{a,ellipse}\tilde{v}_{b,ellipse}}{\sqrt{\tilde{v}_{a,ellipse}^2(\sin\theta)^2 + \tilde{v}_{b,ellipse}^2(\cos\theta)^2}}. \tag{11}$$

Finally, equations of motion for the hole perimeter can be written for  $t_h \leq t \leq (t_h + 4)$  ms as

$$\begin{aligned} \mathbf{v}_{ellipse}(\theta, t) &= \tilde{v}_{t_h,ellipse}(\theta)(\cos\theta)\hat{x} + \tilde{v}_{t_h,ellipse}(\theta)(\sin\theta)\hat{y}, \\ \mathbf{r}_{ellipse}(\theta, t) &= \{x_{t_h}(\theta)(\cos\theta) + \tilde{v}_{t_h,ellipse}(\theta)(\cos\theta)t\}\hat{x} \\ &\quad + \{y_{t_h}(\theta)(\sin\theta) + \tilde{v}_{t_h,ellipse}(\theta)(\sin\theta)t + \frac{1}{2}\tilde{a}_{y,ellipse}t^2\}\hat{y}. \end{aligned} \tag{12}$$

Figures 11 and 12 show horizontal and vertical tracking data of the hole perimeter for position vectors  $\{\mathbf{r}_{hole}(\theta = 45^\circ, t), \mathbf{r}_{hole}(\theta = 135^\circ, t), \mathbf{r}_{hole}(\theta = 225^\circ, t), \mathbf{r}_{hole}(\theta = 315^\circ, t)\}$ , respectively. The dashed lines represent results obtained using Eqn. 12 for the ellipse model of hole

expansion. Figure 13 shows the height and width of the hole obtained from the position tracking data in Fig. 4.

### 4.2 Hole eccentricity

We express the hole eccentricity,  $e_{hole}(t)$ , as a function of hole height,  $h_{hole}(t)$ , and hole width,  $h_{width}(t)$ , as

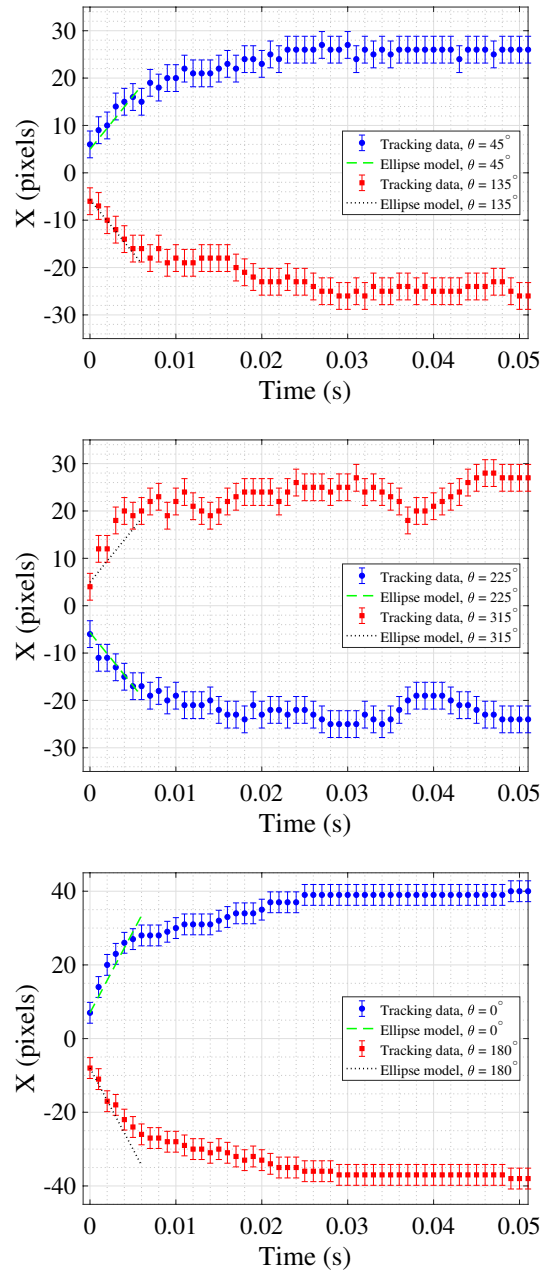
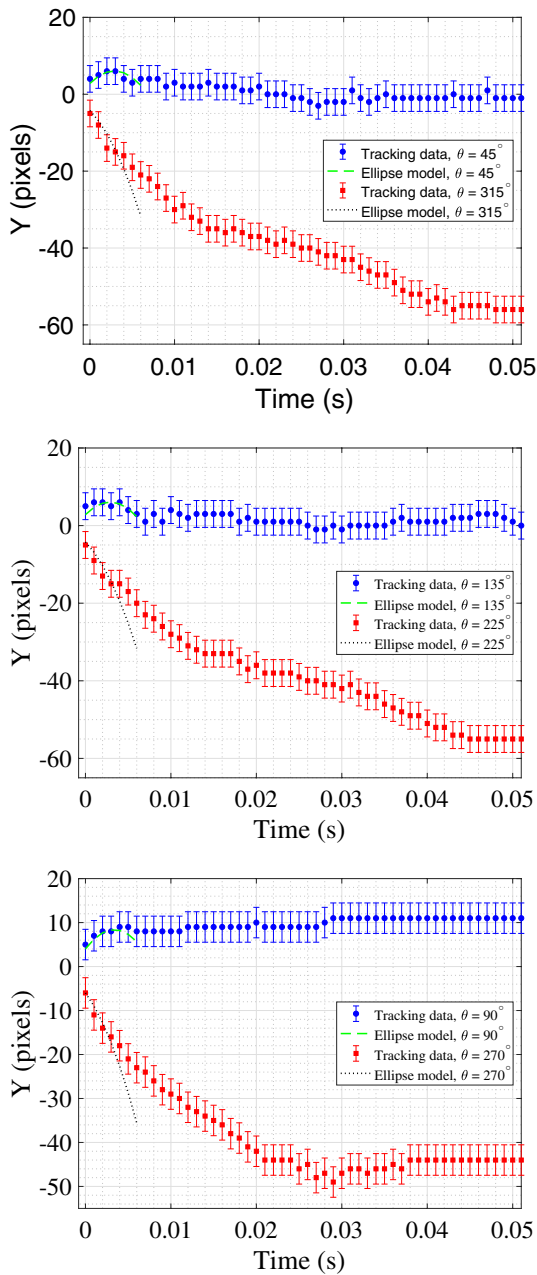
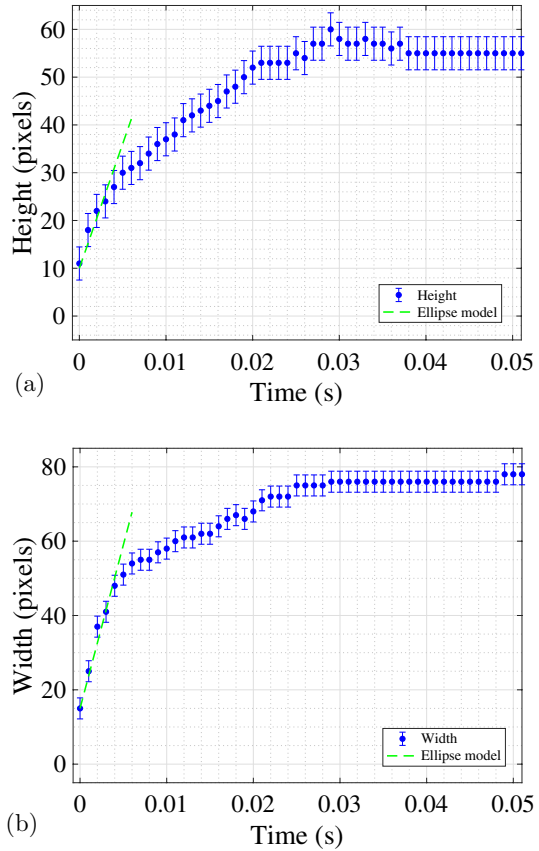


Fig. 11 Horizontal tracking data at hole perimeter for  $\theta = \{0^\circ, 45^\circ, 90^\circ, 135^\circ, 180^\circ, 225^\circ, 270^\circ, 315^\circ\}$ . Dashed lines represent predictions of ellipse model of hole expansion



**Fig. 12** Vertical tracking data at hole perimeter for  $\theta = \{0^\circ, 45^\circ, 90^\circ, 135^\circ, 180^\circ, 225^\circ, 270^\circ, 315^\circ\}$ . Dashed lines represent predictions of ellipse model of hole expansion

$$\begin{aligned}
 e_{\text{hole}}(t) &= \sqrt{1 - \frac{h_{\text{hole}}^2(t)}{w_{\text{hole}}^2(t)}} \\
 &= \sqrt{1 - \frac{\left\{y_{\text{hole}}(\theta = 270^\circ, t) - y_{\text{hole}}(\theta = 90^\circ, t)\right\}^2}{\left\{x_{\text{hole}}(\theta = 180^\circ, t) - x_{\text{hole}}(\theta = 0^\circ, t)\right\}^2}}.
 \end{aligned}
 \tag{13}$$



**Fig. 13** **a** Height and **b** width of hole obtained from measured tracking data (solid blue circles) and predictions of the ellipse model of hole expansion (green dashed lines)

Table 4 shows measured values of the hole eccentricity,  $e_{\text{hole}}(t)$ , obtained from the position tracking data and predictions obtained from the ellipse model of hole expansion in Fig. 13. Figure 14 and Table 4 show that the predictions show very good agreement with measurements calculated from the tracking data.

### 4.3 Hole area

The area of the hole,  $A_{\text{hole}}(t)$ , can be written as functions of the length of the semi-major axis,  $a_{\text{hole}}(t) = \frac{w_{\text{hole}}(t)}{2}$ , and length of the semi-minor axis,  $b_{\text{hole}}(t) = \frac{h_{\text{hole}}(t)}{2}$ , according to the expression,

$$A_{\text{hole}}(t) = \pi a_{\text{hole}}(t) b_{\text{hole}}(t), \tag{14}$$

$$= \pi \frac{w_{\text{hole}}(t)}{2} \frac{h_{\text{hole}}(t)}{2}, \tag{15}$$

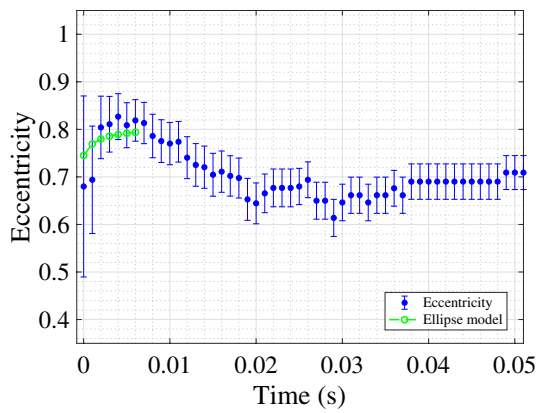


**Fig. 14** Eccentricity of hole obtained from measured tracking data (solid blue circles) and predictions of the ellipse model of hole expansion (green dashed lines)

**Table 4** Hole eccentricity  $e_{\text{hole}}(t)$  as a function of time

Time	$e_{\text{hole}}(t)$ Measurement data	$e_{\text{hole}}(t)$ Ellipse model
$t_h$	$0.680 \pm 0.171$	0.745
$(t_h + 1)$ ms	$0.694 \pm 0.102$	0.769
$(t_h + 2)$ ms	$0.804 \pm 0.061$	0.780
$(t_h + 3)$ ms	$0.811 \pm 0.054$	0.786
$(t_h + 4)$ ms	$0.827 \pm 0.045$	0.789

$$= \frac{\pi}{4} \left( x_{\text{hole}}(\theta = 180^\circ, t) - x_{\text{hole}}(\theta = 0^\circ, t) \right) \left( y_{\text{hole}}(\theta = 270^\circ, t) - y_{\text{hole}}(\theta = 90^\circ, t) \right), \tag{16}$$

where  $x_{\text{hole}}(\theta = 180^\circ, t)$  and  $x_{\text{hole}}(\theta = 0^\circ, t)$  represent x-coordinates of the hole width, and  $y_{\text{hole}}(\theta = 270^\circ, t)$  and  $y_{\text{hole}}(\theta = 90^\circ, t)$  represent y-coordinates of the hole height, respectively.

The standard deviation in the hole area,  $\sigma_{A_{\text{hole}}}(t)$ , can be calculated from the variance,  $\sigma_{A_{\text{hole}}}^2(t)$ , as

$$\begin{aligned} \sigma_{A_{\text{hole}}}(t) &= \sqrt{\sigma_{A_{\text{hole}}}^2(t)}, \\ &= \sqrt{\sigma_{a_{\text{hole}}}^2 \left[ \frac{\partial A_{\text{hole}}(t)}{\partial a_{\text{hole}}(t)} \right]^2 + \sigma_{b_{\text{hole}}}^2 \left[ \frac{\partial A_{\text{hole}}(t)}{\partial b_{\text{hole}}(t)} \right]^2}, \\ &= \sqrt{\sigma_{a_{\text{hole}}}^2 [\pi b_{\text{hole}}(t)]^2 + \sigma_{b_{\text{hole}}}^2 [\pi a_{\text{hole}}(t)]^2}, \\ &= \sqrt{2\pi^2(4.0b_{\text{hole}}^2(t) + 9.0a_{\text{hole}}^2(t))}. \end{aligned} \tag{17}$$

where the uncertainty in the in the semi-major axis,  $a_{\text{hole}} = 2.0\sqrt{2}$ , and semi-minor axis,  $b_{\text{hole}} = 3.0\sqrt{2}$ , is estimated from the tracking data. Figure 15 shows the area of the hole (solid blue circles) as a function of time as obtained from measurement position tracking data. Predictions

obtained from the ellipse model are shown as the dashed green line.

### 4.4 Hole perimeter

In 1914, Srinivasa Ramanujan [99]- [102] provided an approximation (I) for the perimeter of an ellipse,  $P_{\text{hole},1}(t)$ , as

$$P_{\text{hole},1}(t) = \pi \left\{ 3[a_{\text{hole}}(t) + b_{\text{hole}}(t)] - \sqrt{[3a_{\text{hole}}(t) + b_{\text{hole}}(t)][a_{\text{hole}}(t) + 3b_{\text{hole}}(t)]} \right\}. \tag{18}$$

The standard deviation in the perimeter of the hole,  $\sigma_{P_{\text{hole},1}}(t)$ , for this approximation can be calculated from the variance,  $\sigma_{P_{\text{hole},1}}^2(t)$ , as

$$\begin{aligned} \sigma_{P_{\text{hole},1}}(t) &= \sqrt{\sigma_{P_{\text{hole},1}}^2(t)}, \\ &= \sqrt{\sigma_{a_{\text{hole}}}^2(t) \left[ \frac{\partial P_{\text{hole},1}(t)}{\partial a_{\text{hole}}(t)} \right]^2 + \sigma_{b_{\text{hole}}}^2(t) \left[ \frac{\partial P_{\text{hole},1}(t)}{\partial b_{\text{hole}}(t)} \right]^2}, \end{aligned} \tag{19}$$

where the partial derivatives,  $\frac{\partial P_{\text{hole},1}(t)}{\partial a_{\text{hole}}(t)}$  and  $\frac{\partial P_{\text{hole},1}(t)}{\partial b_{\text{hole}}(t)}$ , are given by,

$$\begin{aligned} \frac{\partial P_{\text{hole},1}(t)}{\partial a_{\text{hole}}(t)} &= 3\pi - \frac{\pi}{2} \left\{ \frac{6a_{\text{hole}}(t) + 10b_{\text{hole}}(t)}{\sqrt{3a_{\text{hole}}^2(t) + 10a_{\text{hole}}(t)b_{\text{hole}}(t) + 3b_{\text{hole}}^2(t)}} \right\}, \\ \frac{\partial P_{\text{hole},1}(t)}{\partial b_{\text{hole}}(t)} &= 3\pi - \frac{\pi}{2} \left\{ \frac{6b_{\text{hole}}(t) + 10a_{\text{hole}}(t)}{\sqrt{3a_{\text{hole}}^2(t) + 10a_{\text{hole}}(t)b_{\text{hole}}(t) + 3b_{\text{hole}}^2(t)}} \right\}. \end{aligned} \tag{20}$$

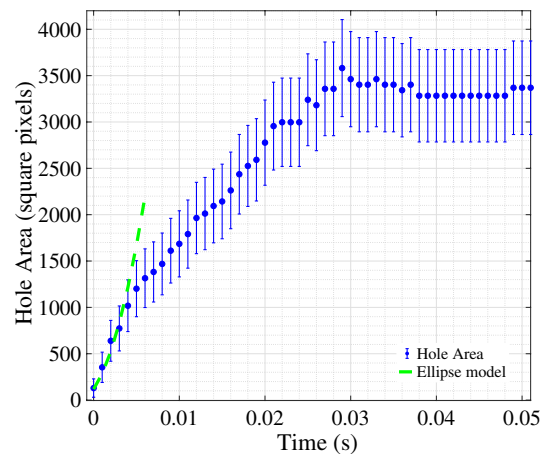


**Fig. 15** Hole area (solid blue circles) obtained from measurement position tracking measurement data and predictions obtained from ellipse model (dashed green line) with one-sigma error bars

Ramanujan [99]- [102] provided a second approximation (II) for the perimeter of the hole  $P_{hole,2}(t)$ ,

$$P_{hole,2}(t) = \pi[a_{hole}(t) + b_{hole}(t)] \left\{ 1 + \frac{3h_{hole}(t)}{10 + \sqrt{4 - 3h_{hole}(t)}} \right\}, \tag{21}$$

where the term,  $h_{hole}(t)$ , is given by the expression,

$$h_{hole}(t) = \frac{[a_{hole}(t) - b_{hole}(t)]^2}{[a_{hole}(t) + b_{hole}(t)]^2}. \tag{22}$$

The standard deviation in the perimeter,  $\sigma_{P_{hole,2}}(t)$ , for this approximation can be calculated from the variance,  $\sigma_{P_{hole,2}}^2(t)$ , where

$$\begin{aligned} \sigma_{P_{hole,2}}(t) &= \sqrt{\sigma_{P_{hole,2}}^2(t)}, \\ &= \sqrt{\sigma_{a_{hole}}^2(t) \left[ \frac{\partial P_{hole,2}(t)}{\partial a_{hole}(t)} \right]^2 + \sigma_{b_{hole}}^2(t) \left[ \frac{\partial P_{hole,2}(t)}{\partial b_{hole}(t)} \right]^2}, \end{aligned} \tag{23}$$

where the partial derivatives,  $\frac{\partial P_{hole,2}(t)}{\partial a_{hole}(t)}$  and  $\frac{\partial P_{hole,2}(t)}{\partial b_{hole}(t)}$ , are given by the expressions,

$$\begin{aligned} \frac{\partial P_{hole,2}(t)}{\partial a_{hole}(t)} &= \frac{2[a_{hole,2}(t) + b_{hole,2}(t)][a_{hole,2}(t) - b_{hole,2}(t)]}{[a_{hole,2}(t) + b_{hole,2}(t)]^4} \\ &\quad - \frac{2[a_{hole,2}(t) - b_{hole,2}(t)]^2[a_{hole,2}(t) + b_{hole,2}(t)]}{[a_{hole,2}(t) + b_{hole,2}(t)]^4}, \\ \frac{\partial P_{hole,2}(t)}{\partial b_{hole}(t)} &= \frac{-2[a_{hole,2}(t) + b_{hole,2}(t)]^2[a_{hole,2}(t) - b_{hole,2}(t)]}{[a_{hole,2}(t) + b_{hole,2}(t)]^4} \\ &\quad - \frac{2[a_{hole,2}(t) - b_{hole,2}(t)]^2[a_{hole,2}(t) + b_{hole,2}(t)]}{[a_{hole,2}(t) + b_{hole,2}(t)]^4}. \end{aligned} \tag{24}$$

Figure 16a and b shows the perimeter of the hole obtained from position measurement tracking data and predictions of the ellipse model (green dashed line) using (a) Ramanujan I and (b) Ramanujan II.

### 4.5 Hole circularity

The hole circularity,  $f_{hole}(t)$ , can be written as functions of the hole area,  $A_{hole}(t)$ , and hole perimeter,  $P_{hole}(t)$ , as,

$$f_{hole}(t) = \frac{4\pi A_{hole}(t)}{P_{hole}^2(t)}. \tag{25}$$

For a circle with width  $w_{circle}(t)$ , the circularity takes on a value of unity,

$$\begin{aligned} f_{circle}(t) &= \frac{4\pi A_{circle}(t)}{P_{circle}^2(t)}, \\ &= \frac{4\pi\pi w_{circle}^2(t)}{[2\pi w_{circle}(t)]^2}, \\ &= 1. \end{aligned} \tag{26}$$

The standard deviation in the hole circularity,  $\sigma_{f_{hole}}(t)$ , can be calculated from the variances in the area,  $\sigma_{A_{hole}}^2(t)$ , and perimeter,  $\sigma_{P_{hole}}^2(t)$ , respectively,

$$\begin{aligned} \sigma_{f_{hole}}(t) &= \sqrt{\sigma_{f_{hole}}^2(t)}, \\ &= \sqrt{\sigma_{A_{hole}}^2(t) \left[ \frac{\partial f_{hole}(t)}{\partial A_{hole}(t)} \right]^2 + \sigma_{P_{hole}}^2(t) \left[ \frac{\partial f_{hole}(t)}{\partial P_{hole}(t)} \right]^2}, \\ &= \frac{4\pi}{P_{hole}^2(t)} \sqrt{\sigma_{A_{hole}}^2(t) + \sigma_{P_{hole}}^2(t) \left[ \frac{A_{hole}^2(t)}{P_{hole}^2(t)} \right]}, \end{aligned} \tag{27}$$

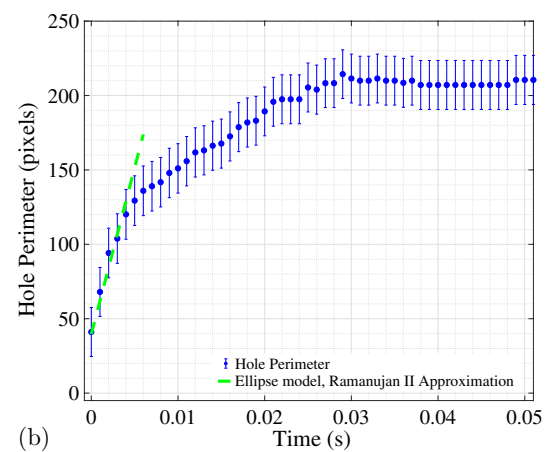
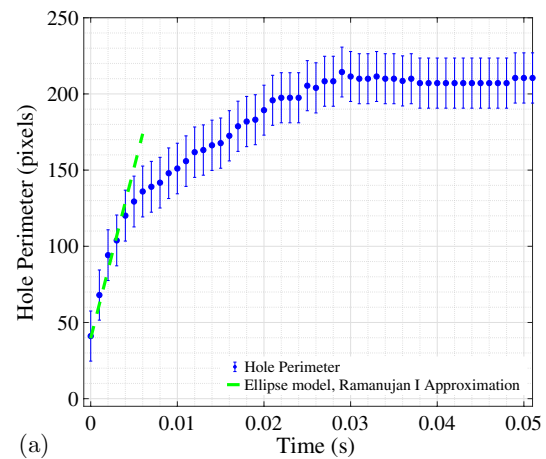


Fig. 16 Perimeter of hole obtained from measured tracking data and model predictions with a Ramanujan I, b Ramanujan II (green dashed lines)

where  $\frac{\partial f_{\text{hole}}(t)}{\partial A_{\text{hole}}(t)} = \frac{4\pi}{P_{\text{hole}}^2(t)}$ , and  $\frac{\partial f_{\text{hole}}(t)}{\partial P_{\text{hole}}(t)} = -\frac{4\pi A_{\text{hole}}(t)}{P_{\text{hole}}^3(t)}$ .

Now, using Ramanujan I, Eqns. 25 and 27 can be written as

$$f_{\text{hole},1}(t) = \frac{4\pi A_{\text{hole}}(t)}{P_{\text{hole},1}^2(t)}, \tag{28}$$

and

$$\sigma_{f_{\text{hole},1}}(t) = \frac{4\pi}{P_{\text{hole},1}^2(t)} \sqrt{\sigma_{A_{\text{hole}}}^2(t) + \sigma_{P_{\text{hole},1}}^2(t) \left[ \frac{A_{\text{hole}}^2(t)}{P_{\text{hole},1}^2(t)} \right]}. \tag{29}$$

With Ramanujan II, Eqns. 25 and 27 can be written as

$$f_{\text{hole},2}(t) = \frac{4\pi A_{\text{hole}}(t)}{P_{\text{hole},2}^2(t)}, \tag{30}$$

and

$$\sigma_{f_{\text{hole},2}}(t) = \frac{4\pi}{P_{\text{hole},2}^2(t)} \sqrt{\sigma_{A_{\text{hole}}}^2(t) + \sigma_{P_{\text{hole},2}}^2(t) \left[ \frac{A_{\text{hole}}^2(t)}{P_{\text{hole},2}^2(t)} \right]}. \tag{31}$$

Figure 17a and b shows the hole circularity (solid blue circles) obtained with approximations of the perimeter provided by Ramanujan I and Ramanujan II, respectively, and position measurement tracking data. The values obtained using predictions of the ellipse model are shown in dashed green lines in each figure. The figures show that the values of the hole circularity obtained with the measurement data show very good agreement with the values obtained with the model predictions for both approximations to the perimeter. The results show that the values of the hole circularity also decrease in the very initial stage of the hole expansion, and this trend is also predicted by the ellipse model.

### 5 Conclusion

In summary, this paper presents the formation of a single liquid drop of molten steel followed by rapid freezing of the molten steel neck upon cooling to room temperature. The drop falls under gravity and oscillates as surface tension tends to make the drop round. The paper also proposes a kinematic model of hole expansion for the very early stages in the bursting of the hole. Research on the hole morphology with this model provides estimates of physical properties of the hole, including hole eccentricity, hole area, hole perimeter, and hole circularity. Future work aims to gain a greater fundamental understanding of the reason that molten liquid drains preferentially at the front face of the steel sheet. See the supplementary material for hole formation,

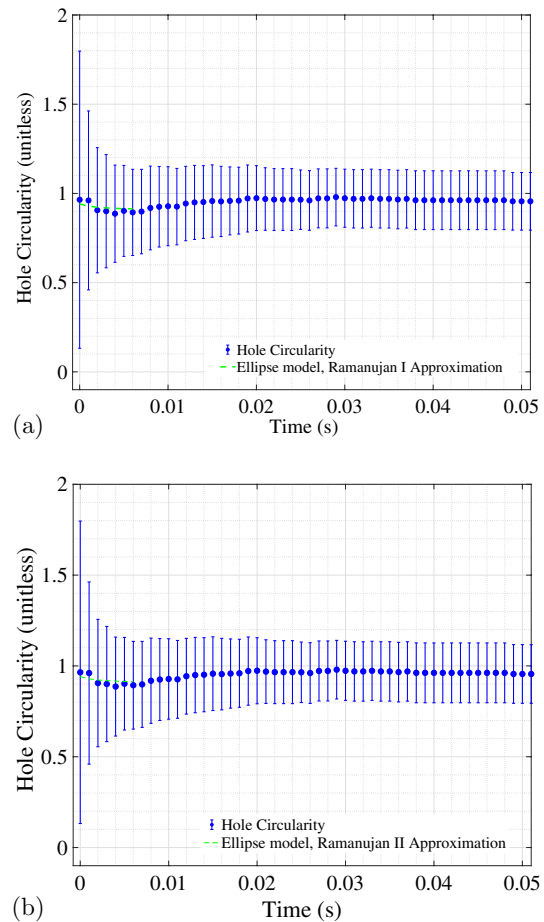


Fig. 17 Circularity of hole obtained from measured tracking data and predictions of the ellipse model of hole expansion

drop formation, and the falling drop with tracking using MotionStudio software (My-Movie-25).

**Electronic supplementary material** The online version of this article (<https://doi.org/10.1007/s00339-021-04680-w>) contains supplementary material, which is available to authorized users.

**Acknowledgements** The views expressed herein are those of the authors and do not reflect the position of the United States Military Academy, the Department of the Army, or the Department of Defense. M. Lanzerotti thanks Norah Stapleton (US Army) for bringing to her attention phase transitions in the 2019 paper “How soap bubbles freeze” by S. F. Ahmadi, S. Nath, C. M. Kingett, P. Yue, and J. B. Boreyko, in *Nature Communications* [103] and thanks J. B. Boreyko for discussions of the units (1/s) for the Rayleigh frequency in Eqn. 1.1 in [90]. M. Lanzerotti thanks K. Sutherland and A. Pinos (both at IDT Vision) for support with MotionStudio software; C. Gerving, T. Book, J. Capps, P. Chapman, B. Huff, T. Halverson, D. Phillips, and D. Kashinski (USMA) for discussions; J. Bishop and Z. Lachance (USMA) for assistance operating the laser and for cutting the steel sheets in the machine shop; and J. Bluman, R. Ellingsen, J. Keena, R. Wilson, and K. Meyer for support of USMA Department of Civil and Mechanical Engineering and measurements of deflection of the steel plates after drop formation and cooling to room temperature.

M. Lanzerotti, K. Allen, and J. Hartke acknowledge the Photonics Research Center, USMA, ARO, DE-JTO.

## References

- John Keats (1818) "LXV. - To Mrs. Wylie," *Letters of Keats, Project Gutenberg*, ["yet was back in time to save one drop of water being spilt."]
- John Keats (1819) "XCVI. - To Joseph Severn," *Letters of Keats, Project Gutenberg*, ["- what a drop of water in the ocean is a Miniature."]
- Miklós Szakáll, Subir K. Mitra, Karoline Diehl, Stephan Borrmann, Shapes and oscillations of falling raindrops: a review. *Atmos. Res.* **97**(4), 416–425 (2010)
- Stalactite. [Online]. Available: <https://en.wikipedia.org/wiki/Stalactite>
- W. Thomson (Lord Kelvin) (1862) "On the secular cooling of the earth. *Proc. Roy. Soc. Edinburgh*, 4: 610-611
- W. Thomson, (Lord Kelvin), On the rigidity of the earth; shift-ings of the earth's instantaneous axis of rotation; and irregulari-ties of the earth as a timekeeper. *Phil. Trans. Roy. Soc. Lond.* **153**, 573–582 (1863)
- W. Thomson, (Lord Kelvin), "On the age of the earth,." *Nature* **51**, 438–440 (1895)
- W. Thomson, (Lord Kelvin), The age of the earth as an abode fitted for life. *Jnl. Trans. Victoria Institute* **31**, 11–35 (1899)
- Philip C. England, Peter Molnar, Frank M. Richter, Kelvin, perry and the age of the earth. *Am. Sci.* **95**(4), 342–349 (2007)
- G. Cummins, M.P.Y. Desmulliez, Inkjet printing of conductive materials: a review. *Circuit World* **38**(4), 193–213 (2012)
- R.C. Tolman, The effect of droplet size on surface tension. *Jnl. Chem. Phys.* **17**(3), 333–337 (1949)
- I. Egly, Surface tension measurements of liquid metals by the oscillating drop technique. *Jnl. Mat. Sci.* **26**, 2997–3003 (1991)
- B. Vinet, J.P. Garandet, L. Cortella, Surface tension measure-ments of refractory liquid metals by the pendant drop method under ultrahigh vacuum conditions: Extension and comments on Tate's law. *Jnl. Appl. Phys.* **73**, 3830–3834 (1993)
- J. Juza, The pendant drop method of surface tension measure-ment: equation interpolating the shape factor tables for several selected planes. *Czechoslovak Jnl. Phys.* **47**(3), 351–352 (1997)
- O.E. Yildirim, Q. Xu, O.A. Basaran, Analysis of the drop weight method. *Phys. Fluids* **17**, 062107 (2005)
- B. Lautrup, "Surface tension," Ch. 5 in "Physics of continuous matter: Exotic and everyday phenomena in the macroscopic world," The Niels Bohr Institute, Denmark, pp. 73, 1998–2010. <https://www.routledge.com/Physics-of-Continuous-Matter-Exotic-and-Everyday-Phenomena-in-the-Macroscopic/Lautrup/book/9780367865115>
- J.D. Berry, M.J. Neeson, R.R. Dagastine, D.Y.C. Chan, R.F. Tabor, Measurement of surface and interfacial tension using pendant drop tensiometry. *Jnl. Colloid Interface Sci.* **454**, 226–237 (2015)
- R. P. Woodward, Surface tension measurements using the drop shape method. First ten angstroms
- A. Vaks, O.S. Gutareva, S.F.M. Breitenbach, E. Avirmed, A.J. Mason, A.L. Thomas, A.V. Osinzev, A.M. Kononov, G.M. Henderson, Speleothems reveal 500,000-year history of Siberian permafrost. *Science* **340**, 183–186 (2013)
- A. Da Silva, J. Volpp, J. Frostevarg, A.F.H. Kaplan, Acceleration of metal drops in a laser beam. *Appl. Phys. A* **127**(4), 1–13 (2021)
- N. Bowering, C. Meier, Sticking behavior and transformation of tin droplets on silicon wafers and multilayer-coated mirrors. *Appl. Phys. A* **125**(9), 1–12 (2019)
- H. Brüning, F. Vollertsen, Form filling behaviour of preforms generated by laser rod end melting. *Lasers Manuf. Conf.* **2015**, 10 (2015)
- E. Govekar, A. Jeri, M. Weigl, M. Schmidt, Laser droplet generation: application to droplet joining. *CIRP Ann. Manuf. Technol.* **58**, 205 (2009)
- A. Kuznetsov, A. Jeromen, E. Govekar, C.I.R.P. Ann, Manuf. Technol. **63**, 225 (2014)
- M. Gatzen, T. Radel, C. Thomy, F. Vollertsen, Wetting behavior of eutectic Al Si droplets on zinc coated steel substrates. *J. Mater. Process. Technol.* **214**, 123 (2014)
- B. Bizjan, A. Kuznetsov, A. Jeromen, E. Govekar, B. Sirok, High-speed camera thermometry of laser droplet generation. *Appl. Thermal Eng.* **110**(5), 298–305 (2017)
- J.P. Oliveira, Z. Zeng, Laser welding. *Metals* **9**, 69 (2019). <https://doi.org/10.3390/met9010069>
- M. Shome, M. Tumuluru, *Welding and Joining of Advanced High Strength Steels (AHSS)*" (Woodhead Publishing, Cambridge, 2015)
- E. Sinkora, "Traditional Versus Laser Welding," *SME Media*, October 28, 2019. [Online]. Available: <https://www.sme.org/technologies/articles/2019/october/traditional-versus-laser-welding/>
- "Laser Welding & Durable Design: How Our Customer Made More than 5 Million Products in 5 Years," December 16, 2018. [Online]. Available: <https://facteon.global/news/laser-welding-and-durable-design-how/>
- D. Maudlin, L. O'Neill, I. De Mallie, F. Arnold, L.A. Florence, J. Hartke, D.O. Kashinski, J.E. Johnson, J. Lamb, R. Huffman, D.E. Riegner, N.F. Fell, T. Kreidler, G. Tamm, N.F. Fell, Effects of rotation and inert thermal sinks on laser heating of cold, rolled-steel cylinders: preliminary experimental results. *Jnl. Dir. Energy* **6**, 198–208 (2017)
- J. Broussard, N. Hedglin, T. Le, P. Meyers, T. Halverson, M. Lanzerotti, K. Ingold, D. Kashinski, J. Harke, "Experimental Measurement of Hole Formation in Metal as a Function of Angle of Incidence from a HEL," 20th Annual Directed Energy Science & Technology Symposium (DEPS) 2018, Oxnard, CA, Feb. 26 - Mar. 2, 2018
- J. Kazmi, S. Joiner, J. Broussard, D. Brewster, D. Kashinski, M. Lanzerotti, J. Hartke, "Engaging Steel Coupons with High Energy Lasers: Analysis of Full-Beam Penetration Time as a Function of Orientation," 21st Annual Directed Energy Science & Technology Symposium (DEPS) 2019, Destin, FL, April 8-12, 2019
- ATHENA Laser weapon system prototype. [Online]. Available as of May 30, 2021: <https://www.lockheedmartin.com/en-us/products/athena.html/>
- Rheinmetall, MBDA building high-energy lasers for Germany's Navy. [Online]. Available as of May 30, 2021: <https://www.defensenews.com/global/europe/2021/01/28/rheinmetall-mbda-building-high-energy-lasers-for-germanys-navy/>
- Q. Lehua, H. Yi, L. Jun, Z. Daicong, S. He, Embedded printing trace planning for aluminum droplets depositing on dissolvable supports with varying section. *Robot. Comput. Integr. Manu.* **63**, 101898 (2020)
- H. Yi, L.-H. Qi, J. Luo, Y. Jiang, W. Deng, Pinhole formation from liquid metal microdroplets impact on solid surfaces. *Appl. Phys. Lett.* **108**, 041601 (2016)
- H. Yi, L. Qi, J. Luo, D. Zhang, H. Li, X. Hou, Intl. Jnl. Mach. Tools Manu. **130–131**, 1–11 (2018)

39. Leonardo da Vinci, *The Notebooks of Leonardo Da Vinci: Arranged, Rendered into English and Introduced by Edward MacCurdy*, vol. 1 (Reynal & Hitchcock, New York, 1938)
40. Leonardo da Vinci, *The Notebooks of Leonardo Da Vinci: Arranged, Rendered into English and Introduced by Edward MacCurdy*, vol. 2 (Reynal & Hitchcock, New York, 1938)
41. Codex Arundel - - Leonardo notebook (Highlights) + Codex Arundel (full notebook)
42. British Library. Contents: Notebook of Leonardo da Vinci ("The Codex Arundel"), 1478-1518
43. Edmé Mariotte, *Traité du mouvement des eaux et des autres corps fluides, divisé en V parties, par feu M. Mariotte, mis en lumière par les soins de M. de La Hire* E. Michallet, Paris, 1686. Translated into English by John Theophilus Desaguliers, *The Motion of Water and Other Fluids: Being a Treatise of Hydrostatics* London: J. Senex and W. Taylor, 1718. Goutte d'eau is mentioned on pp. 30, 34, 120, 198, 278 (goutte d'eau étoit tombée dans un certain temps), 296, 298
44. J. C. Maxwell, "Capillary action," *Encyclopaedia Britannica*
45. P. S. Laplace, *Traité de Méchanique Céleste, Tome Quatrième, Supplément au livre X*, Tension is mentioned on pp. 69 and p. 77, 1805. [Online]. Available: <https://archive.org/details/traidumouvemen01marigoog/page/n7/mode/2up>
46. T. Young, III. An essay on the cohesion of fluids. *Phil. Trans. R. Soc. Lond* **95**, 65–87 (1805)
47. Felix Savart, "Mémoire sur la constitution des veines liquides lancées par des orifices circulaires en mince paroi," *Annales de Chimie*, vol. 53, no. 337, 1833
48. J. M. W. Bush, "Interfacial phenomena, Ch. 13, Fluid Sheets," MIT OCW: 18.357 Interfacial Phenomena, pp. 49-54, Fall 2010
49. T. Tate, On the magnitude of a drop of liquid formed under different circumstances. *Phil. Mag. S. 27*(181), 176–180 (1864)
50. A.M. Worthington, *A Study of Splashes* (Longmans, Green, and Co., USA, 1908)
51. H.E. Edgerton, E.A. Hauser, W.B. Tucker, Studies in drop formation as revealed by the high-speed motion camera. *J. Phys. Chem.* **41**(7), 1017–1028 (1937)
52. D. J. K. Stuart, "Analysis of Reynolds Number Effects in Fluid Flow through Two-dimensional Cascades," *Aeronautical Res. Council Rep. and Memoranda.*, R. & M. No. 2920 (15, 260) A. R. C. Technical Report. 1955
53. D.H. Peregrine, G. Shoker, A. Symon, The bifurcation of liquid bridges. *J. Fluid Mech.* **212**, 25–39 (1990)
54. E. Becker, W.J. Hiller, T.A. Kowalewski, Experimental and theoretical investigation of large amplitude oscillations of liquid droplets. *Jnl. Fluid Mech.* **231**, 189–210 (1991)
55. E. Becker, W.J. Hiller, T.A. Kowalewski, Nonlinear dynamics of viscous droplets. *Jnl. Fluid Mech.* **258**, 191–216 (1994)
56. J. Eggers, Universal pinching of 3D axisymmetric free-surface flow. *Phys. Rev. Lett.* **71**(21), 3458–3460 (1993)
57. J. Eggers, T.F. Dupont, Drop formation in a one-dimensional approximation of the Navier-Stokes equation. *J. Fluid Mech.* **262**, 205–221 (1994)
58. J. Eggers, Theory of drop formation. *Phys. Fluids* **7**, 941 (1995)
59. J. Eggers, Drop formation - an overview. *ZAMM - Z. Angew. Math. Mech.* **85**(6), 400–410 (2005)
60. J. Eggers, Post-breakup solutions of Navier-Stokes and Stokes threads. *Phys. Fluids* **26**, 072104 (2014)
61. J. Eggers, M.A. Fontelos, *Singularities: Formation, Structure, and Propagation* (Cambridge University Press, Cambridge, 2015)
62. X.D. Shi, M.P. Brenner, S.R. Nagel, A cascade of structure in a drop falling from a faucet. *Science* **265**, 219–222 (1995)
63. X. Zhang, O.A. Basaran, An experimental study of dynamics of drop formation. *Phys. Fluids* **7**(6), 1184–1203 (1995)
64. O. B. Fawehinmi, P. H. Gaskell, P. K. Jimack, N. Kapur, H. M. Thompson A combined experimental and computational fluid dynamics analysis of the dynamics of drop formation. *Proc. IMechE, Part. C: J. Mech. Eng. Sci.*, 219: 1-15 (2005)
65. V. Grubelnick, M. Marhl, Drop formation in a falling stream of liquid. *Am. J. Phys.* **73**(5), 415–419 (2005)
66. H. Dong, W.W. Carr, J.F. Morris, An experimental study of drop-on-demand drop formation. *Phys. Fluids* **18**, 072102 (2006)
67. D.M. Henderson, W.G. Pritchard, L.B. Smolka, On the pinch-off of a pendant drop of viscous fluid. *Phys. Fluids* **9**, 3188 (1997)
68. A. Haenlein, "Disintegration of a liquid jet," *Forschung auf dem Gebiete des Ingenieurwesens*, vol. III, no. 4, April 1931. Technical Memorandums, National Advisory Committee for Aeronautics, No. 659, Washington, DC, Feb. 1932
69. E.F. Goedde, M.C. Yuen, Experiments on liquid jet instability. *J. Fluid Mech.* **40**, 495–511 (1970)
70. K.C. Chaudhary, L.G. Redekopp, The nonlinear instability of a liquid jet. Part 1, Theory. *J. Fluid Mech.* **96**(2), 257–274 (1980)
71. K.C. Chaudhary, T. Maxworthy, The nonlinear instability of a liquid jet. Part 2, experiments on jet behavior before droplet formation. *J. Fluid Mech.* **96**(2), 275–286 (1980)
72. K.C. Chaudhary, T. Maxworthy, The nonlinear instability of a liquid jet. Part 3, experiments on satellite drop formation and control. *J. Fluid Mech.* **96**(2), 287–297 (1980)
73. C. Clanet, J.C. Lasheras, Transition from dripping to jetting. *J. Fluid Mech.* **383**, 307–326 (1999)
74. Z. Néda, B. Bakó, E. Rees, The dripping faucet revisited. *Chaos* **6**(1), 59–62 (1996)
75. P. Couillet, L. Mahadevan, C. Riera, Return map for the chaotic dripping faucet. *Prog. Theor. Phys. Supplement* **139**, 507–516 (2000)
76. J. Job, R. Patel, P. N. Pritchard, C. Royer, "The dripping faucet: Investigation of behavior in water droplet formation," Final Paper, Phys. 6268, Georgia Institute of Tech., 2011
77. J. Job, R. Patel, P. N. Pritchard, C. Royer, "Drip Drip 'Til You Drop: An Investigation of Dripping Faucet Dynamics," Final Paper, Phys. 6268, Georgia Institute of Tech., 2011
78. H. Suetani, K. Soijima, R. Matsuoka, U. Partitz, H. Hata, Manifold learning approach for chaos in the dripping faucet. *Phys. Fluids* **18**, 072102 (2006)
79. H. Lamb, On the oscillations of a viscous spheroid. *Proc. Lond. Math. Soc.* **13**(1), 51–70 (1881)
80. William Thomson (Lord Kelvin), "Oscillations of a liquid sphere," pp. 384-386, 1890
81. J. W. Strutt (Lord Rayleigh), "On the capillary phenomena of jets," *Proc. Roy. Soc. London*, vol. 29, pp. 71-97, 1897
82. J. W. Strutt (Lord Rayleigh), "Some Applications of Photography," *Proc. Roy. Inst. Great Britain*, vol. 13, pp. 261-273, 1891. Also in *Nature*, vol. 44 (1133), pp. 249-254
83. S. Chandrasekhar, The oscillations of a viscous liquid globe. *Proc. London Math. Soc.* **3**, 141–149 (1959)
84. S. Chandrasekhar, *Hydrodynamic and Hydromagnetic Stability* (Clarendon Press, Oxford, 1961), pp. 466–477
85. W.H. Reid, The oscillations of a viscous liquid drop. *Quart. Appl. Math.* **18**, 86–89 (1960)
86. G. Thorsen, R.M. Stordalen, S.G. Terjesen, On the terminal velocity of circulating and oscillating liquid drops. *Chem. Eng. Sci.* **23**, 413–426 (1968)
87. C.A. Morrison, R.P. Leavitt, D.E. Wortman, The extended Rayleigh theory of the oscillation of liquid droplets. *Jnl. Fluid Mech.* **104**, 295–309 (1981)
88. M. Perez, Y. Brechet, L. Salvo, M. Papoular, M. Suery, Oscillation of liquid drops under gravity: influence of shape on the resonance frequency. *Europhys. Lett.* **47**(2), 189–195 (1999)

89. T. Matsumoto, H. Fujii, T. Ueda, M. Kamai, K. Nogi, Oscillating drop method using a falling droplet. *Rev. Sci. Instru.* **75**, 1219 (2004)
90. D. V. Lyubimov, V. V. Konovalov, T. P. Lyubimova, I. Egry, Small amplitude shape oscillations of a spherical liquid drop with surface viscosity. *Jnl. Fluid Mech.* **677**, 1–14 (2011). <https://doi.org/10.1017/jfm.2011.76>.
91. C. López, A. Hirsra, Fast focusing using a pinned-contact oscillating liquid lens. *Nature Photon* **2**, 610–613 (2008)
92. S.K. Ramalingam, O.A. Basaran, Axisymmetric oscillation modes of a double droplet system. *Phys. Fluids* **22**, 112111 (2010)
93. C.F. Tilger, J.D. Olles, A.H. Hirsra, Phase behavior of oscillating double droplets. *Appl. Phys. Lett.* **103**, 264105 (2013). <https://doi.org/10.1063/1.4858487>
94. T.S. Eliot, “Little Gidding,” September, 1942. [“*Between melting and freezing The soul's sap quivers.*”]
95. M. Lanzerotti, K. Brakke, K. Allen, J. Hartke, Bursting of molten steel thick films in a steel plate illuminated by a high energy laser. *Appl. Phys. Lett.* **115**, 115043702 (2019)
96. T. Nishizuka, Y. Sato, T. Takamizawa, K. Sugisawa, and T. Yamamura, in *Proc. 16th European Conf. on Thermophysical Properties*, Imperial College, London, 2002
97. K. Morohoshi, M. Uchikoshi, M. Isshiki, H. Fukuyama, Surface Tension of Liquid Iron as Functions of Oxygen Activity and Temperature. *ISIJ Intl.* **51**(10), 1580–1586 (2011)
98. M. Gugliotti, M.S. Baptista, M.J. Politi, Surface tension gradients induced by temperature: the thermal Marangoni effect. *Jnl. Chem. Educ.* **81**(6), 824–826 (2004)
99. Mark B. Villarino, “Ramanujan’s Perimeter of an Ellipse,” February 1, 2008. <https://arxiv.org/pdf/math/0506384.pdf>
100. Paul Bourke, “Circumference of an Ellipse Collected by Paul Bourke, Corrections and contributions by David Cantrell and Charles Karney,” updated June 2013
101. Stanislav Sykora, “Approximations of Ellipse Perimeters and of the Complete Elliptic Integral E(x). Review of known formulae,” December 27, 2005
102. Paul Abbott, “On the Perimeter of an Ellipse,” Online. Available: <http://paulbourke.net/geometry/ellipsecirc/Abbott.pdf>
103. S.F. Ahmadi, S. Nath, C.M. Kingett, P. Yue, J.B. Boreyko, How soap bubbles freeze. *Nature Comm.* **10**(2531), 1–9 (2019). <https://doi.org/10.1038/s41467-019-10021-6>

**Publisher’s Note** Springer Nature remains neutral with regard to jurisdictional claims in published maps and institutional affiliations.